Isotope Effect of Rovibrational Distribution of Hydrogen Molecules Desorbed from Amorphous Carbon

Hiroaki Nakamura[1,2*], Seiki Saito[3], Takumi Sawada[2], Keiji Sawada[4], Gakushi Kawamura[1,5], Masahiro Kobayashi[1,5] and Masahiro Hasuo[6]

[1]*National Institute for Fusion Science, Oroshi-cho, Toki, Gifu 509-5292, Japan*

[2]*Nagoya University, Furo-cho, Nagoya 464-8601, Japan*

[3]*Yamagata University, 4-3-16 Jonan, Yonezawa, Yamagata 992-8510, Japan*

[4]*Shinshu University, 4-17-1 Wakasato, Nagano 380-8553, Japan*

[5] *The Graduate University for Advanced Studies, SOKENDAI, Oroshi-cho, Toki, Gifu 509-5292, Japan*

[6]*Kyoto University, Kyotodaigaku-katsura, Nishikyo-ku, Kyoto 615-8540, Japan*

When the hydrogen isotope atom is injected to the amorphous carbon with the incident energies E_{in} of 20, 50, and 80 eV, we obtain the following physical quantities of hydrogen isotope atoms/molecules emitted from the amorphous carbon using molecular dynamics and heat conduction hybrid simulation, The physical quantities are the time evolution of the emission rate, the depth distribution of the original location of the hydrogen emitted from the target, the polar angular dependence, and the translational, rotational, and vibrational energy distributions. In addition, the approximate analysis yields the emission distributions at the vibrational (v) and rotational (J) levels. Using these distributions, we evaluate the rotational temperature T_{rot} for $v = 0$ and small J states. From the above, it is found that molecules with higher rotational levels J tend to be emitted as E_{in} increases or as the mass of hydrogen isotope increases. Moreover, the isotope effect appears in the mass dependence of T_{rot}.

1. Introduction

We have been studying transportation of the neutral particles, *e.g.,* hydrogen atoms or molecules, in the plasma.[1–3] The purpose of the study is to reveal the mechanism of the detached plasma, which is one of candidates to decrease the heat load to the divertor to realize nuclear fusion generation.[4] Hsu, *et al.* performed the pioneering experiment of the detached plasma using their divetor simulation device.[5] Led by their experiment, the basic experiments were carried out in linear plasma devices,[6–8] and the understanding of the detached plasma was advanced. Furthermore, the detached plasma experiments in tokamak[9–12] or helical[13] devices have also been advanced and these findings have been incorporated into the ITER.[14]

The plasma recombination plays an essential role in the detached plasma which reduces

*E-mail:hnakamura@nifs.ac.jp

particle and heat flux to the divertor plate.[15] The spectra analysis by Ohno, *et al.* shows that the molecular assisted recombination (MAR) process involving vibrationally excited hydrogen molecules as well as the radiative and three-body recombination is important.[16–18] In the MAR process, the information of the neutral particles, especially hydrogen atoms and molecules around peripheral region are necessary. To study the neutral transport phenomena, one of the authors K.S. has been developing a neutral-transport (NT) code,[1,19] which includes a rovibrationally resolved collisional-radiative (CR) model of molecular hydrogen. In our previous work,[1] using the NT-CR code, we tracked hydrogen atoms and molecules released from the graphite divertor target, assuming a divetor plasma in the large helical device (LHD). In this work, the initial rovibrational state of the molecular hydrogen released from the graphite divertor target was simulated using the molecular dynamics and heat conduction (MD-HC) hybrid code we developed.[2] This MD-HC code was initially developed for the irradiation of carbon materials with "light hydrogen atom" because it was intended for the graphite divetor target of LHD, but it was later improved for the irradiation of tungsten.[3]

Here, we make a comment on the carbon assumed as the target material in the MD-HC code. Carbon has seen important advances in carbon science, including chemical vapor deposition (CVD) of diamond, fullerenes, carbon nanotubes, single-walled graphene, and even amorphous carbon, *e. g.*, diamond-like carbon[20] (DLC). Recently, intrinsic DLCs and doped DLCs have been investigated electrochemically, especially as electrode materials used in electroanalysis.[21]

On the other hand, plasma confinement experiments were carried out using deuterium in LHD, and the isotope effects were reported.[22,23] Motivated by these isotope experiments at LHD, we aim to extend the NT-CR and the MD-HC codes, which had been developed for light hydrogen, to handle not only deuterium but also tritium. These isotope experiments at LHD motivated us to extend the NT-CR and MD-HC codes, which had been developed for light hydrogen (H), to handle not only deuterium (D) but also tritium (T). Our MD-HC code has the potential to be used for DLC.

In this paper, we concentrate on the isotopic hydrogen molecules which are emitted from the carbon wall. We reveal the isotope effect of emission from carbon amorphous.

2. Hybridization of Molecular Dynamics Simulation and Heat Conduction Equation

2.1 Simulation model

We used the same simulation method as our previous work.[2,3] Therefore, the simulation model (Fig.1), which is almost the same as the previous simulation, consists of two regions,

i.e., the molecular dynamics (MD) region and the heat conduction (HC) region as in the previous work.

2.1.1 Setup of MD region Figure 2 shows the simulation model of the MD region in the case of H. First, we prepared, as a target for each H, D and T, a unit structure with10 Å × 10 Å × 30 Å of amorphous carbon containing hydrogen isotope atoms by the following steps:[2)] (i) In the initial state, an amorphous carbon structure containing excess hydrogen isotope atoms is prepared; (ii) After annealing the cell, excess hydrogen isotope atoms are removed by annealing. Thus, we obtained the unit structure for each H, D and T as shown in Fig. 2(a) which contains 242 carbons and 130 hydrogen isotopes.

Next, making 16 copies of the unit structure and arranging them as shown in Fig. 2(b), we construct the target structure for each H, D and T whose size is 40 Å × 40 Å × 30 Å. There are 3,872 carbons and 2,080 hydrogen isotopes in the target for each H, D and T, which corresponds to H/C = D/C = T/C ∼ 0.53. The density of carbon atoms in the target was obtained from our previous MD simulation of depositing carbon atoms to form the amorphous carbon.[24)]

We note that the hydrogen concentration H/C for carbon deposited layers in experiments depends critically on the energy of the incident hydrogen flux, and energetic ions lead to the deposition of hard films with hydrogen concentrations H/C of about 0.4, while low energy thermal hydrogen leads to the formation of soft films, with H/C concentrations exceeding 1.[25–30)] The periodic boundary condition is adopted in the $x-$ and $y-$directions.

Moreover, we comment on treating the hydrogen isotopes, *i.e.,* light hydrogen (H), deuterium (D), tritium (T). In each simulation model, carbon atoms and only one type of hydrogen isotope are considered. In other words, we do not assume a mixed system in which two or more of H, D and T exist simultaneously throughout this work.

2.1.2 Setup of HC region The heat conduction (HC) region surrounds the MD region as shown in Fig.1. The whole system is divided with cubic cells with one side of 6.67 Å. The HC region connects the MD region through the connecting region.

2.2 Simulation method

In the previous works,[3)] we have developed the MD simulation which includes the effect of heat transfer to the bulk by solving heat conduction (HC) equation. We named this simulation MD-HC hybrid simulation. In Fig. 1, we show the schematic diagram of the MD-HC hybrid simulation. The details of the MD-HC hybrid simulation are shown in Ref.3 and consequently only a brief overview of the MD-HC hybrid simulation will be given below.

2.2.1 MD simulation including hydrogen isotope injection In § 2.1.1, we created the initial structure of the target for each case of H, D, and T. In other words, three targets were prepared in total. One atom of hydrogen isotope is irradiated to the target corresponding to the type of the injected isotope. The time evolution of the carbon atoms and hydrogen isotopes in the target is then simulated. The irradiation method is described in detail below. We inject one hydrogen isotope atom to the shaded square, *i.e.*, "incident area" along the z axis from a distance 10 Å above the surface of the target (see Fig. 2). The $x-$ and $y-$coordinates of the initial position of the incident hydrogen isotope, *i.e.,* $(x_{\rm in}, y_{\rm in}, z_{\rm in} = -10\text{Å})$ are set randomly in the region of 15 Å $< x_{\rm in} <$ 25 Å and 15 Å $< y_{\rm in} <$ 25 Å as shown in Fig. 2(b). We adopt three values, *i.e.*, 20, 50 and 80 eV as the incident kinetic energy $E_{\rm in}$. For each type and incident kinetic energy for the injected isotope, we perform 1,500 trials changing $(x_{\rm in}, y_{\rm in})$ in the target corresponding to the type of the injected isotope from the three initial targets. The initial temperature of all targets is set to 300 K.

Here, we comment on the relationship between the initial structure of the target and the atoms and molecules generated from the target. It is expected that the generated atoms and molecules depend on the distribution of carbon and hydrogen isotopes in the initial target. However, the correlation between the initial structure and the generated particles has not been investigated in detail using computer simulations. As a first step in determining this relationship, we will investigate the generated particles by focusing on only one structure for each isotope.

In the MD simulation, the time integration of the equation of the motion for all atoms in the MD region including incident a hydrogen isotope atom are executed numerically under *NVE* ensamble using a second-order symplectic integration.[31] The time step Δt is 0.02 fs. The periodic boundary condition is used in the MD simulation for the $x-$ and the $y-$ directions. The modified reactive empirical bond order (REBO) potential[32] is used as the interaction between all atoms. In the MD simulation, the REBO potential functions developed for "light hydrogen" (H) is directly applied to deuterium (D) and tritium (T). The difference among hydrogen isotopes atoms is mass as follows: The masses of H, D and T are 1.00782503207, 2.0141017778 and 3.0160492777, respectively, whose unit are unified atomic mass unit.

After the MD simulation is performed for one step, i.e., $\Delta t = 0.02$ fs, we calculate the temperature of each cell in "connecting region" (Fig. 1) and move on to calculation of the HC equation (§. 2.2.2).

2.2.2 HC equation As the next step of the MD simulation (§. 2.2.1), we solve the following heat conduction (HC) equation in the HC region in Fig. 1.

$$\frac{\partial T_{\rm cell}(i,j,k)}{\partial t} = \alpha \Delta T_{\rm cell}(i,j,k), \tag{1}$$

where the thermal diffusivity α is 3.93×10^{-7} m^2/s.[3] $T_{\rm cell}(i,j,k)$ is the temperature of the cell (i,j,k) in the HC region. The boundary condition of Eq. (1) is set as follows: We fix the outermost surface, which is filled with blue in Fig.1, to $T_{\rm cell\ at\ outer\ surface}$ =300 K. $\partial T_{\rm cell}/\partial z|_{\rm upper\ surface} = 0$ at the upper surface in Fig.1(b), which is filled with black. Integrating Eq. (1) with the same time step as in the MD simulation, i.e., $\Delta t = 0.02$ fs, we obtain a new $T^{\rm new}_{\rm cell}(i,j,k)$ for each cell at the next time step.

2.2.3 Repetition with MD simulation and HC equation Using $T^{\rm new}_{\rm cell}(i_{\rm cc}, j_{\rm cc}, k_{\rm cc})$ in each connecting cell $(i_{\rm cc}, j_{\rm cc}, k_{\rm cc})$ (Fig.1), we multiply the momenta of all atoms in each connecting cell $(i_{\rm cc}, j_{\rm cc}, k_{\rm cc})$ by the amplitude $\sqrt{T^{\rm new}_{\rm cell}(i_{\rm cc}, j_{\rm cc}, k_{\rm cc})/T_{\rm cell}(i_{\rm cc}, j_{\rm cc}, k_{\rm cc})}$. Using the new momenta of the atoms in the connecting cells, we perform the MD simulation for $\Delta t = 0.02$ fs and integrate the HC equation (1) again.

Repeating the above MD simulation (§. 2.2.1) and the HC equation (§. 2.2.2) for 250,000 times, which corresponds to 50 ps, we obtain the time evolution of both the motion of all atoms in the MD region and the temperature in the HC region, respectively.

Using thermal equilibrium, we validated our MD-HC hybrid simulation in our previous work.[2]

3. Simulation Results and Discussions

We have performed the MD-HC hybrid simulations for three hydrogen isotope atoms (H, D, T) with the three incident kinetic energy $E_{\rm in}$ = 20, 50 and 80 eV. In each case, we take the statistical average by 1,500 trials changing the incident position of the projectile in Fig.2, as already mentioned in §2.2.1.

3.1 General behavior of emission

We consider the case of light hydrogen H. We define the incident hydrogen as $H^{\rm in}$ and the hydrogen located in the target at the initial state as $H^{\rm t}$. Injected $H^{\rm in}$ collides with other atoms ($H^{\rm t}$ or carbon C) in the target several times. During the collisions, the incident kinetic energy of $H^{\rm in}$ is transfered to $H^{\rm t}$ or C. After several collisions among $H^{\rm in}$, $H^{\rm t}$ and C, the following atoms/molecules eventually are emitted from the surface of the target:

- the incident hydrogen atom ($H^{\rm in}$).
- hydrogen atoms which are located in the target ($H^{\rm t}$).

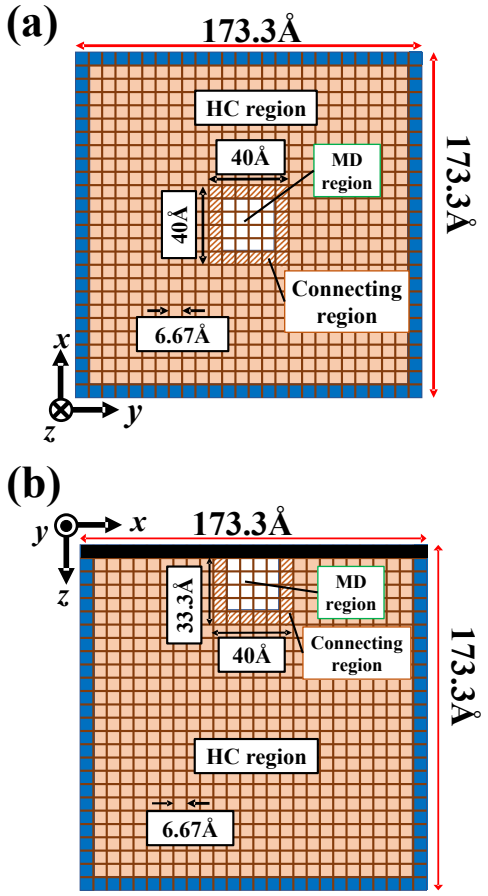

Fig. 1. The schematic diagram of MD-HC hybrid simulation model. (a) The xy and (b) the xz cross sections of the simulation system. We fix the outermost surface, which is filled with blue, to $T_{\text{cell at outer surface}}$ =300 K. $\partial T_{\text{cell}}/\partial z|_{\text{upper surface}} = 0$ at the upper surface in (b), which is filled with black. The cells in the HC region are labeled as (i, j, k). In particular, only cells in the connecting region are added a subscript "cc" as $(i_{\text{cc}}, j_{\text{cc}}, k_{\text{cc}})$.

- hydrogen molecules including the incident hydrogen (H^{in}-H^{t}).
- hydrogen molecules without the incident hydrogen (H_2^{t}).
- hydrocarbon molecules (C_l-H_m^{t} or C_l-H^{in}-H_m^{t}, where l is a positive integer and m is a non-negative integer.)

The above is a summary of light hydrogen H. The same argument can be made for deuterium D and tritium T.

3.2 Time evolution of emission rate

Performing the MD-HC hybrid simulation, we obtain the time evolution of the emitted atoms/molecules for each hydrogen isotopes accumulated every 0.01ps in Fig.3. In this figure, we've distinguished emitted hydrogen isotopes by whether the isotopes were injected or not. Regardless of types of hydrogen isotopes (H, D or T), the hydrogen isotopes are emitted along

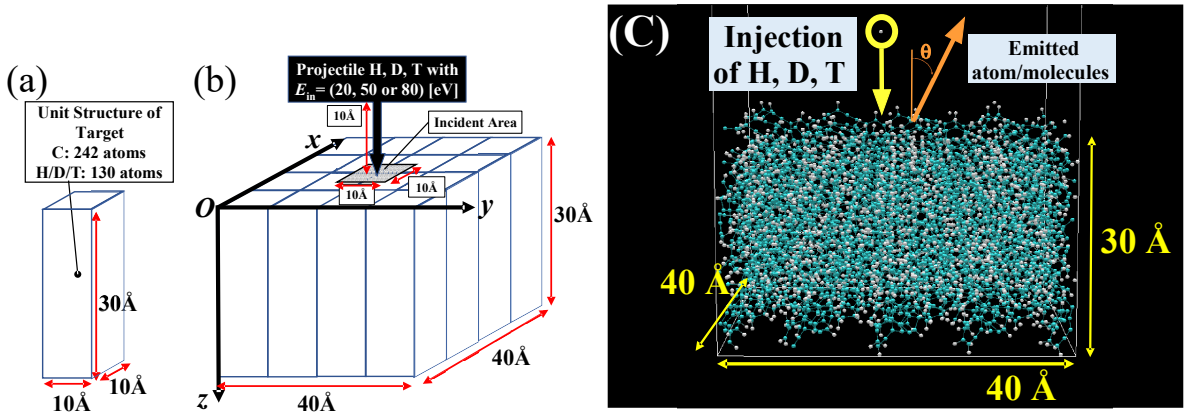

Fig. 2. Simulation model in the MD region. This MD region is surrounded by the heat conduction (HC) region as shown in Fig.1. (a) The unit structure of the MD region which consists of 242 carbon and 130 hydrogen isotope atoms. (b) Schematic diagram of the MD region which is created by arranging 4×4 replicated unit structures. (c) The projectile, *i.e.,* H, D or T, with the incident kinetic energy E_{in} = 20, 50 or 80 eV, is injected from 10 Å above the surface along the $z-$ axis. The direction of the emitted atoms/molecules is defined by the polar angle θ as shown in the figure. The blue and white balls denote the carbon and hydrogen isotope atoms, respectively.

the time sequence as follows.

- Below 0.1 ps, all incident hydrogen isotopes (H^{in}, D^{in} and T^{in}) have an emission peak.
- Around 0.1 ps, the hydrogen isotopes that were originally located in the carbon receive kinetic energy from the incident atoms and are emitted from the surface of the target.
- Approximately at the same time as the emission of the hydrogen isotopes that are located originally in the carbon, molecules are also emitted from the target.
- The emission rate of molecules is smaller than those of atoms, but it continues for at least 50 ps.

From Fig.3, we also found the difference among H, D and T as follows: as the mass of isotopes increases, the amount of emitted atoms decreases for all E_{in}. This behavior can be explained as follows: in each simulation model, two types of particles collide: one is hydrogen isotope and the other is carbon. It is known[33] that the kinetic energy of the incident atom is transferred most efficiently when the masses of the two colliding particles are the same. Hence, for a collision between a hydrogen isotope atom and a carbon atom, the kinetic energy of the incident atom transfer increases as the mass of the hydrogen isotope atom approaches the carbon atom. For these reasons, the incident particles lose kinetic energy and have difficulty escaping from the target. For the above reasons, the incident particle loses its kinetic energy and has difficulty escaping from the target. As a result, the amount of the incident particles

emitted decreases as its mass increases.

Next, we analyze the incident kinetic energy dependence of emission rate. When the kinetic energy of the incident particle increases, the amount of the incident particle itself (backscattering rate) tends to become smaller. The reason for this behavior is considered as follows: The higher the incident energy is, the deeper the incident particle penetrates into the target and loses their kinetic energy. For the above reason, there is not enough kinetic energy left to return from the deep end to the target surface again and therefore the amount of incident particles emitted is reduced.

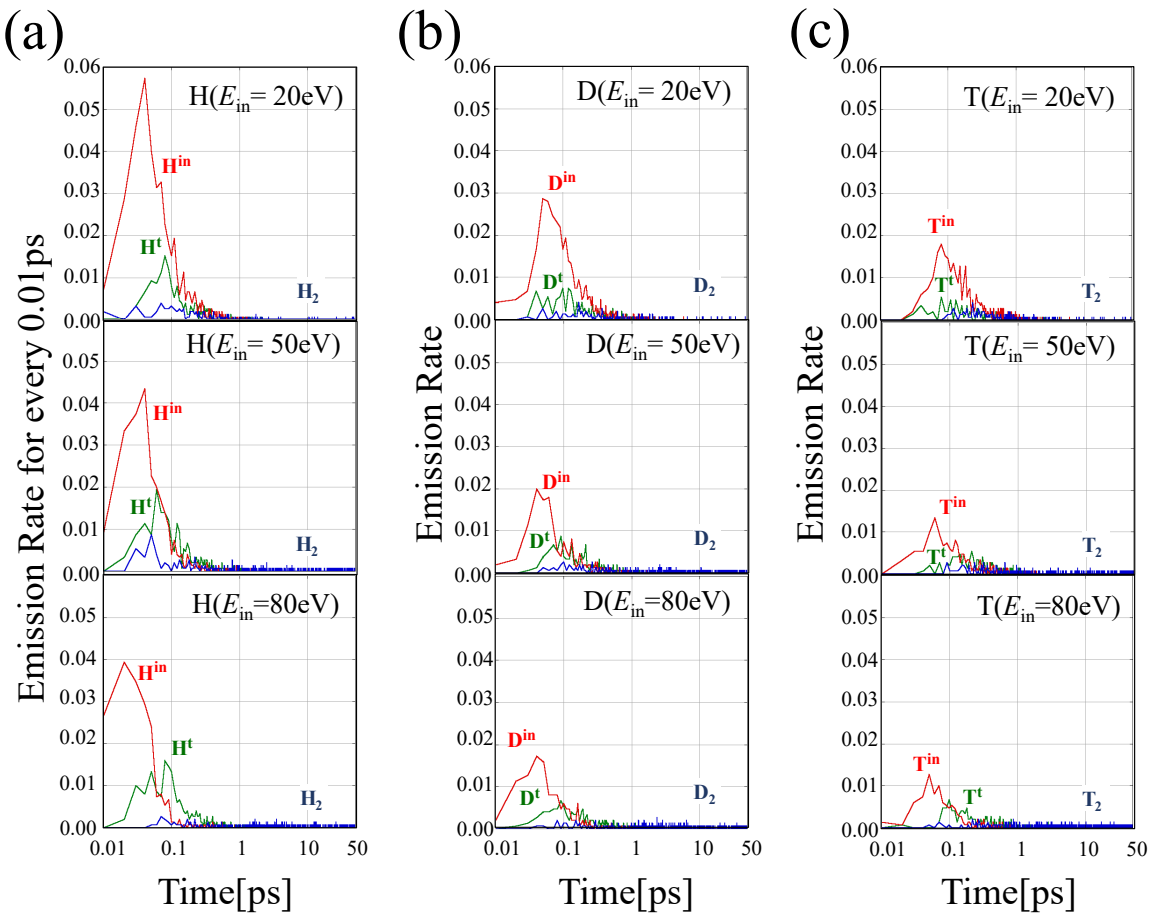

Fig. 3. Time evolution of the emission rate, which is the ratio of how many particles were emitted out of 1,500 trials during each 0.01 ps for (a) light hydrogen H, (b) deuterium D and (c) tritium T. The superscript "in" (red) indicates that the injected atom was emitted. On the other hand, the superscript "t" (green) indicates that the emitted atom was originally in a target. Isotope molecules, H_2, D_2 and T_2 are marked in blue. For all hydrogen isotopes, the incident kinetic energies E_{in} are 20, 50 and 80 eV from the top figure to the bottom figure.

3.3 Depth-in-target dependence of emitted particles

As explained in§2.1.1, hydrogen isotopes are initially distributed in the target. The initial positions of the emitted hydrogen atoms/molecules (*i.e.,* H^t or H_2) are expected to depend on the hydrogen distribution in the initial state. In Fig.4, we plot both the initial hydrogen isotopes distribution and the distribution of locations in the target of emitted H^t or emitted H_2.

First, we focus on Fig.4(a)(H), where the upper figure shows the initial depth-distribution of hydrogen atoms in the target and the lower one shows the distribution of the original locations of H^t for $E_{\rm in}$ = 20, 50 and 80 eV. As $E_{\rm in}$ increases, the original locations of H^t is getting deeper. It is also found that the correlation between the original locations of H^t and the initial depth-distribution of hydrogen is not so pronounced.

Second, we explain Fig. 4(b)(H_2), where the upper figure shows the initial depth-distribution of hydrogen molecules in the target and the lower one shows the distribution of the original locations of H_2 for $E_{\rm in}$ = 20, 50 and 80 eV. In the target, a pair of hydrogen atoms whose distance between hydrogen atoms is within twice the distance between hydrogen molecules in a vacuum (2×0.74 Å= 1.48Å) is classified as "molecular hydrogen" in the target.

Third, we compare Fig. 4(a)(H) with Fig. 4(b)(H_2). In Fig. 4(b)(H_2), as $E_{\rm in}$ increases, the original locations of H_2 is getting deeper as same as in the case of H. However, Fig. 4(b)(H_2) confirms that there is a correlation between the original locations of H_2 and the initial depth-distribution of hydrogen molecules in contrast to Fig. 4(a)(H). The above features can be confirmed for D and T as well.

In the last part of this subsection, we consider the mass dependence. Comparing among H, D and T in Fig. 4(a) or (b) respectively, it is difficult to find any mass-dependence of distribution of the emission rate.

3.4 Polar angle θ dependence of emission rate

We also analyze[2)] the polar-angle θ dependence of emission for all hydrogen isotopes, where θ is defined in Fig. 2(c). The data are accumulated for every 5° polar angles. The result of the analysis are plotted in Fig. 5. For the θ dependence, the analysis done in the previous work[2)] is also applied here. When the particles are emitted uniformly, the distribution of the emission angle θ follows $\sin\theta$ curve because it is proportional to the solid angle. In many transport codes, the emission angle θ is generated with the probability proportional to $\cos\theta$. The colored dotted-lines in Fig. 5 show the curves obtained by fitting the simulation data to $\alpha \sin\theta \cos^{\beta}\theta$ which is the distribution when particles are emitted with the probability proportional to $\cos^{\beta}\theta$.

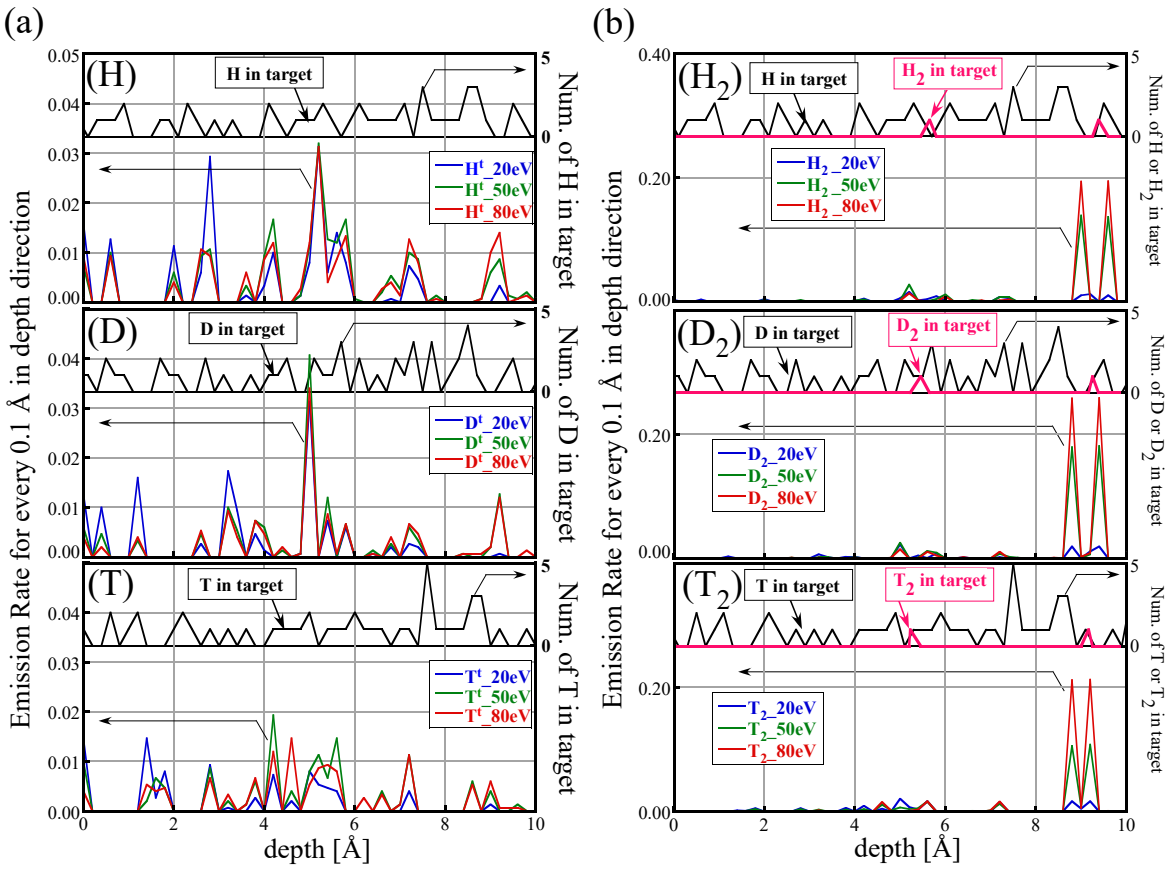

Fig. 4. Hydrogen isotope distributions in the target and the initial depth distribution of the emitted isotope. The emission rate in the figure is the ratio of how many particles were emitted out of 1,500 trials during the entire simulation time 50 ps for every 0.1 Å in the depth direction. The cases of hydrogen atom H, D and T are in (a); the cases of molecules H_2, D_2 and T_2 are in (b). In the target, a pair of hydrogen atoms whose distance between the atoms is within twice the distance between hydrogen molecules in a vacuum (2×0.74 Å$= 1.48$Å) is classified as "hydrogen molecule" in the target. The deuterium and tritium molecule in the target are defined in the same way. In all cases, $E_{\rm in}$ = 20, 50 and 80 eV.

The fitting parameters (α, β) for H, D, and T with $E_{\rm in}$ = 20, 50 and 80 eV are summarized in Table I.

From the figure, we found that the emission rates of the injected atom, *i.e.,* H^{in}, D^{in} or T^{in} decreases as its mass or the incident kinetic energy E^{in} becomes larger as the same as in Fig. 3. However, the mass dependence of the emission rate of the molecules is not so obvious. On the other hand, as the E^{in} increases, more kinetic energy is transferred to the hydrogen atoms in the target, resulting in a larger emission rate of the molecules.

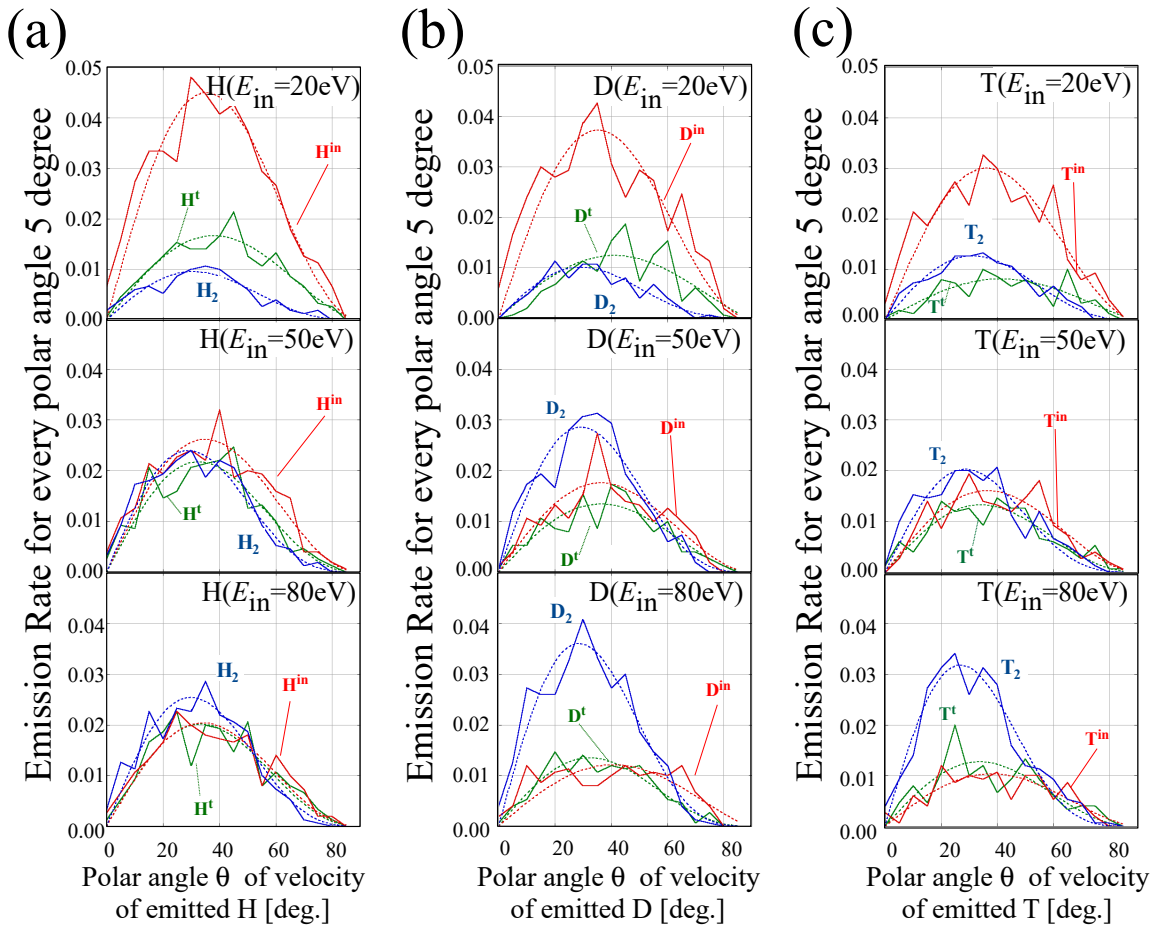

Fig. 5. Polar angle θ dependence of the emission rate for H, D and T. The data are accumulated for every polar angle 5° during the entire simulation time 50 ps. The superscripts "in" and "t" indicate the same meaning as in Fig. 3. The superscript "in" (red solid line) indicates that the injected atom was emitted. On the other hand, the superscript "t" (green solid line) indicates that the emitted atom was originally in a target. Isotope molecules, H_2, D_2 and T_2 are depicted in blue solid lines. The incident kinetic energy E_{in} is set to 20, 50 and 80 eV as in Fig. 3. Each colored dotted-lines show the curves obtained by fitting the simulation data to $\alpha \sin\theta \cos^{\beta}\theta$, where the fitting parameters (α, β) are listed in Table I.

3.5 Energy dependence of emission rate

In this sub-session, the translational, rotational, and vibrational energy distributions of the emission rate are determined for only molecules H_2, D_2, and T_2. Here, we define the translational, rotational, or vibrational energy as E_g, E_{rot} or E_{vib}, respectively. Figure 6 shows the E_g, E_{rot} and E_{vib} distributions for H_2, D_2 and T_2 with E_{in} = 20, 50 and 80 eV. For all isotopes, as E_{in} increases, the emission rates is also larger as in Fig.5. The mass dependence of the distributions is not so clear. Using these distributions, we will show the rovibrational-state distributions of emission rate in §3.6.

Table I. List of the fitting parameters(α, β) in the fitting function $\alpha \sin\theta \cos^{\beta}\theta$ for H, D and T. Abbreviation "in" denotes that the injected hydrogen isotope is reflected; "t" denotes that the isotope atom that was originally in the target is released from the target; "mol." denotes that the hydrogen isotope molecule are released, respectively.

(α, β) in $\alpha \sin\theta \cos^{\beta}\theta$		H	D	T
E_{in}	released particles.	Fig. 5(a)	Fig. 5(b)	Fig. 5(c)
20 eV	in	(0.116, 1.994)	(0.098, 1.999)	(0.075, 1.843)
	t	(0.040, 1.644)	(0.027, 1.314)	(0.017, 1.278)
	mol.	(0.028, 2.825)	(0.031, 3.175)	(0.037, 2.719)
50 eV	in	(0.068, 2.039)	(0.044, 1.856)	(0.040, 1.810)
	t	(0.061, 2.423)	(0.033, 1.848)	(0.035, 2.162)
	mol.	(0.076, 3.248)	(0.090, 3.177)	(0.065, 3.357)
80 eV	in	(0.054, 2.171)	(0.026, 1.346)	(0.024, 1.629)
	t	(0.055, 2.297)	(0.038, 2.477)	(0.034, 2.240)
	mol.	(0.078, 3.012)	(0.116, 3.372)	(0.109, 3.885)

3.6 Rovibrational-state distributions of emission rate

By analyzing the energy distributions obtained in the previous sub-section §3.5 using the approximation method,[2)] we obtain the distributions of the rotational-vibrational levels (abbreviated as "rovibrational" levels) in this sub-section. By inputting the distribution of hydrogen molecules in each rovibrational level obtained here into the neutral transport (NT) code,[1)] we can obtain the propagation of the hydrogen atoms/molecules in the plasma. In other words, the calculation of NT code is highly dependent on the quality of the input distribution of hydrogen from the wall, which is the source of the hydrogen molecules.

Before describing the results, we explain the approximation to obtain the quantum distribution function from the classical distribution function. Originally, in order to obtain the quantum distribution function, the motion of atoms must be solved by quantum mechanics, however, in reality, this is impossible due to the limitations of computers. Therefore, as an alternative, we use the results of classical molecular dynamics simulation. The approximate method to obtain the quantum distribution function from the classical distribution function is simply explained as follows: We label the hydrogen molecule with the energy states (v, J) closest to the rotational and vibrational energies determined by classical MD. Here we use non-negative integers v and J as quantum numbers to represent the vibrational and rotational states, respectively.

In order to obtain the rovibrational-state distribution, the eigenenergy $E_k(v, J)$ for each

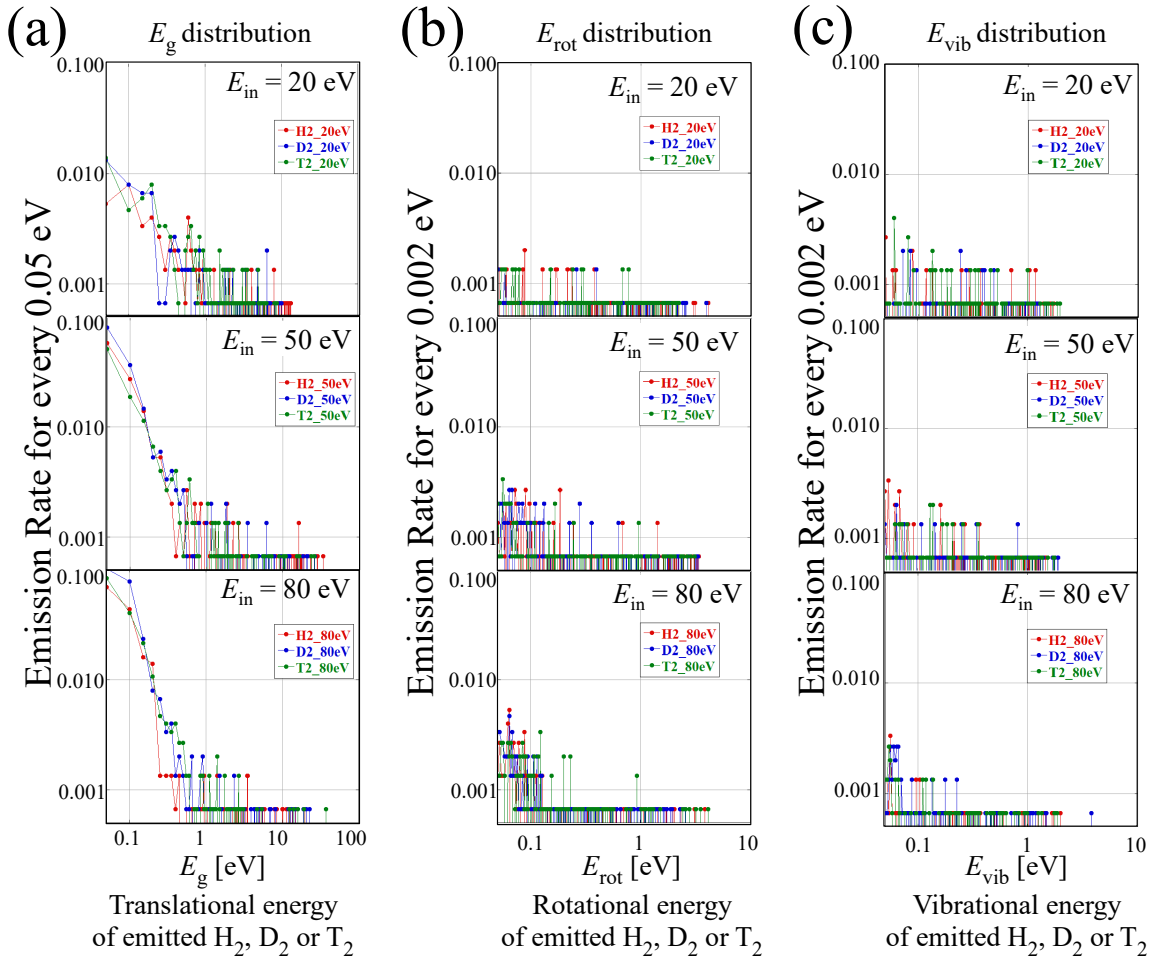

Fig. 6. The translational energy E_g, the rotational E_{rot} and the vibrational energy E_{vib} distributions of the emission rate for H_2 (red), D_2 (blue) and T_2 (green) in the cases of $E_{in} = 20, 50$ and 80 eV for the entire simulation time 50 ps. (a) The data for E_g are accumulated for every 0.05 eV and (b,c) those for E_{rot} and E_{vib} are accumulated for every 0.002 eV.

rovibrational state (v, J) and each kind of isotopes k= H_2, D_2, and T_2, is calculated by solving the following Schrödinger equation of two particle systems with the Numerov method:[2,19,34]

$$\left\{-\frac{\hbar^2}{2\mu_k}\frac{\partial^2}{\partial R^2}\left[V(R)+\frac{2\hbar^2}{2\mu_k}\frac{J(J+1)}{R^2}\right]\right\}\Psi_{kvJ}(R) = E_k(v,J)\Psi_{kvJ}(R), \tag{2}$$

where $\Psi_{kvJ}(R)$ is the eigenfunction for (v, J) state and the isotope k, R is the relative distance between isotopic molecules, and $\hbar$ is the Planck constant divided by 2π. The reduced mass μ_k is given by $m_k/2$, where m_k is the mass of H, D and T. The REBO potential[32] is used as the potential between hydrogen molecules $V(R)$. Some of the eigenenergies $E_k(v, J)$ are summarized in Table II.

In Fig. 7, we plot the J dependence of each emission rate for $v = 0, 1, 2$ or the sum of $v = 0$

Table II. Some of the eigenenergies $E_k(v, J)$ of isotropic hydrogen molecules k= H_2, D_2, and T_2 for the rovibrational state (v, J). The Schrödinger equation (2) is solved numerically with the Numerov method.[34] The REBO potential[32] is used as the potential between hydrogen molecules $V(R)$ in Eq. (2).

(v, J)	$E_{H_2}(v, J)$ [eV]	$E_{D_2}(v, J)$ [eV]	$E_{T_2}(v, J)$ [eV]
(0,0)	-4.457885	-4.53600	-4.57081
(0,1)	-4.443223	-4.52860	-4.56586
(0,2)	-4.414034	-4.51385	-4.55598
(0,3)	-4.370586	-4.49179	-4.54119
(0, 4)	-4.313271	-4.46255	-4.52154
(0, 5)	-4.242590	-4.42624	-4.49709
(0, 6)	-4.159146	-4.38303	-4.46792
(0, 7)	-4.063622	-4.33311	-4.43410
(0, 8)	-3.956770	-4.27668	-4.39575
(0, 9)	-3.839388	-4.21399	-4.35296
(0, 10)	-3.712312	-4.14528	-4.30586
(0, 11)	-3.576395	-4.07083	-4.25458
(0, 12)	-3.432494	-3.99091	-4.19925
(0, 13)	-3.281461	-3.90582	-4.14002
(0, 14)	-3.124125	-3.81585	-4.07704
(0, 15)	-2.961280	-3.72132	-4.01046
(0, 16)	-2.793675	-3.62252	-3.94046
(0, 17)	-2.621994	-3.51977	-3.86718
(0, 18)	-2.446848	-3.41338	-3.79080
(0, 19)	-2.268754	-3.30364	-3.71149
(0, 20)	-2.088126	-3.19087	-3.62941

to 8, which is denoted as "all v". Here we comment that the emission rate becomes negligibly small when $v \geq 8$ as a result of the simulation.

In all cases of H_2, D_2 and T_2, the emission rates tend to increase as the incident energy $E_{\rm in}$ increases. We found that there are a several states of $J \geq 10$ for all isotopes, from the case of "all v" in Fig.7. From Ref.19, it is known that the dissociative attachment rate coefficient for $H_2(X^1\Sigma_g^+, v = 0, J > 0)$ +e $\rightarrow$ $H_2^-(X^2\Sigma_u^+)$ +e $\rightarrow$ H(1)+H^- increases by orders of magnitude large compared to that for $J = 0$. Namely, it is expected that the hydrogen molecules with a large J which are emitted from the target enhance the dissociative attachment. From the present simulations, it is found that hydrogen molecules in high rovibrational states are emitted from the wall. It suggests that the reaction between such hydrogen molecules and the hydrogen plasma is much larger than previously thought.

Next, we discuss the mass dependence. Comparing (a), (b) and (c) in Fig. 7, it is found that the number of states with large J, especially $5 \leq J \leq 10$, increases slightly as the mass increases. This is because the kinetic energy of the incident hydrogen tends to be transferred to the carbon as the mass approaches the mass of the carbon, as discussed in Figs. 3 and 5. The kinetic energy transferred to the carbon is eventually transferred to the hydrogen in the target. In other words, as the kinetic energy of the target obtained from the incident hydrogen becomes larger, the hydrogen in the target becomes more easily excited, and as a result, the rotational states J of emitted hydrogen molecules become higher.

3.7 Rotational temperature

We evaluate the rotational temperature T_{rot} using Fig. 7. From our previous work,[1)] it was found that, in the case that $v = 0$ and J is small, the emission rate $n_k(v, J)$ could be approximated by the following Boltzmann distribution:

$$\frac{n_k(v=0,J)}{2J+1} \propto e^{-\frac{\Delta E_k(0,J)}{k_{\mathrm{B}} T_{\mathrm{rot}}}}, \tag{3}$$

where $\Delta E_k(v, J) := E_k(v, J) - E_k(v, 0)$ and k_{B} is the Boltzmann constant. We replot the emission rate ($v = 0$) divided with $2J + 1$ in Fig. 8. In these figures, the modified emission rates are fitted with Eq. (3) using the least square method. From the slopes of the fitting functions, the rotational temperature and the errors are obtained as shown in Fig. 9. Because the fitting error becomes large for $E_{\mathrm{in}} = 20$ eV, the estimation of T_{rot} is inaccurate. However, the T_{rot} for both $E_{\mathrm{in}} = 50$ and 80 eV decreases as the mass of the molecule increases. This dependence can be qualitatively explained as follows: As the mass of the incident hydrogen isotope is larger and closer to the carbon atom, the momentum of the isotope is more easily transferred to the carbon. As a result, less momentum is transferred to the stored hydrogen isotopes, and the rotational energy of the released isotropic hydrogen molecule is also reduced.

In addition, the T_{rot} for both $E_{\mathrm{in}} = 50$ and 80 eV tends to be higher than the temperature of the target (300K) and, the T_{rot} increases, as the E_{in} becomes larger. This is thought to be due to the fact that the temperature around the surface of the target, where the incident particle strikes, is higher than the initial target temperature (300K), and as a result, the T_{rot} of the released molecular hydrogen is also higher than 300K.

Next, we discuss the deviations from the Boltzmann distribution (3). We invested the released molecules from the time when the graphite target is irradiated with the hydrogen isotope. This phenomenon is in non-equilibrium state because it is essentially transient phenomenon. However, the Boltzmann distribution used in this fitting is defined in equilibrium.

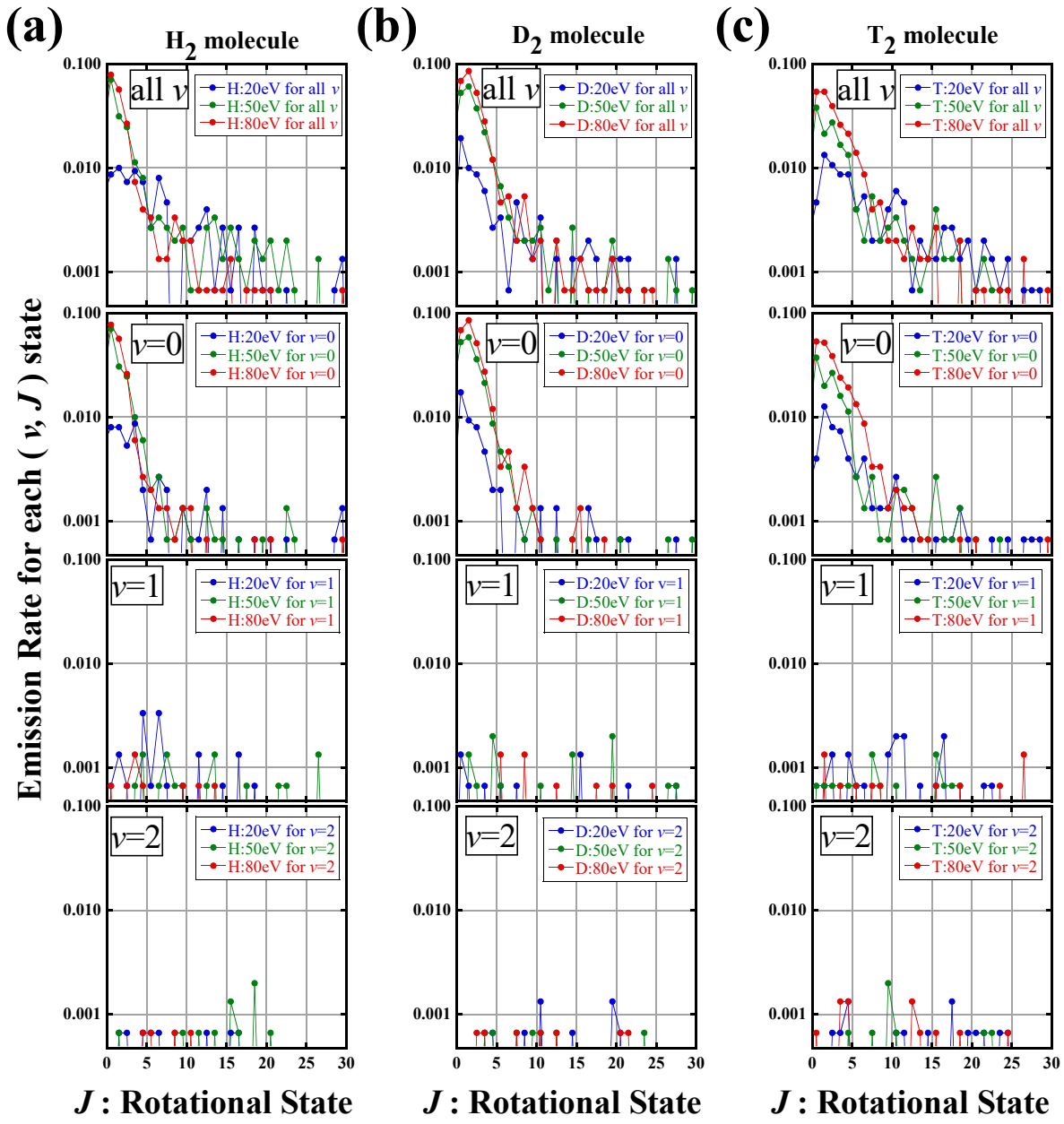

Fig. 7. The rotational state J dependence of the emission rate for each vibrational state $v = 0, 1, 2$ or "all v", which denotes that sum of the emission in the cases of $v = 0$ to 8. Each figure shows the result of (a) H_2, (b) D_2 or (c) T_2, respectively.

From the above, the deviation from the Boltzmann distribution represents the non-equilibrium part of the hydrogen isotope molecule released from graphite. Furthermore, it is found that the non-equilibrium component of the molecular hydrogen isotope emission generates larger J states than expected by the Boltzmann distribution.

Finally, we comment on the vibrational temperature of the molecules. From the cases of $v = 0, 1$ and 2 in Fig. 7, it is found that the emission rates for $v = 2$ and 3 are more than an

order of magnitude smaller than that for $v = 1$. It suggests that the distribution of hydrogen isotope molecules is mostly in the ground state ($v = 0$) of the vibration, and that the excitation to higher states ($v \geq 1$) does not take place enough to be represented by the Boltzmann distribution.

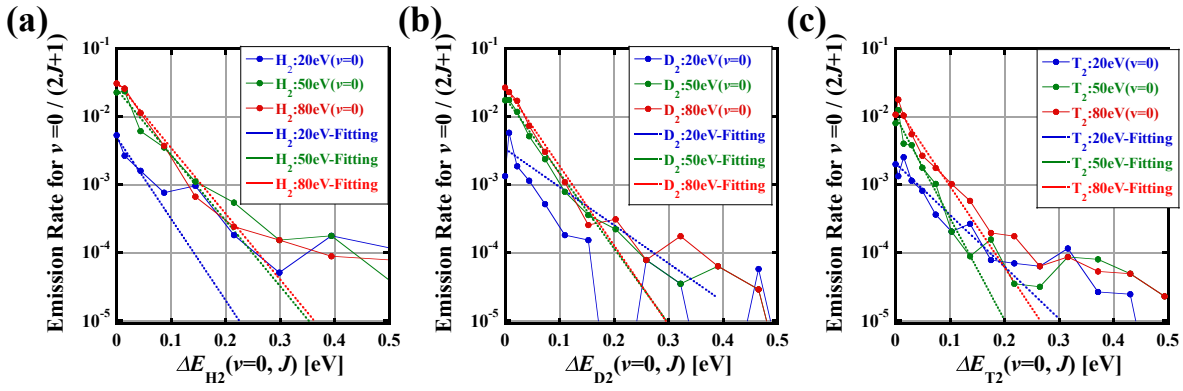

Fig. 8. The emission rate for $v = 0$ divided with $(2J + 1)$ versus $\Delta E_k(0, J) = E_k(0, J) - E_k(v, 0)$. The Boltzmann distribution $\exp[-\Delta E_k(0, J)/(k_B T_{\rm rot})]$ is use as a fitting function. In both cases of $E_{\rm in} = 50$ and 80 eV, fitting with the Boltzmann distributions is well done for small $\Delta E_k(0, J)$. However, in the case of $E_{\rm in} = 20$ eV, fitting is not well done with the Boltzmann distribution.

4. Summary

Using molecular dynamics and heat conduction (MD-HC) hybrid simulation, we calculated the emission rate of hydrogen isotope atoms/molecules emitted from the amorphous carbon including hydrogen isotope atoms when the hydrogen isotope atom is injected to the amorphous carbon.

As a result, the time evolution of the emission rate Fig. 3, the depth distribution of the original location of the hydrogen emitted from the target Fig. 4, the polar angular dependence Fig. 5, and the translational, rotational, and vibrational energy distributions Fig. 6 are obtained for H, D, and T, respectively, at incident energies $E_{\rm in}$ of 20, 50, and 80 eV.

Furthermore, by approximate analysis, the distributions of emission at the rotational and vibrational levels were obtained in Fig.7. From this figure, it was found that molecules with higher rotational levels J tend to be emitted as $E_{\rm in}$ increases or as the mass of hydrogen isotope increases. Moreover, the rotational temperature $T_{\rm rot}$ is evaluated using the emission rates for $v = 0$ and small J in Fig. 9. It suggests that there is an isotope effect on the $T_{\rm rot}$.

The distribution obtained here can be input to the neutral transport (NT) code[1)] to calculate

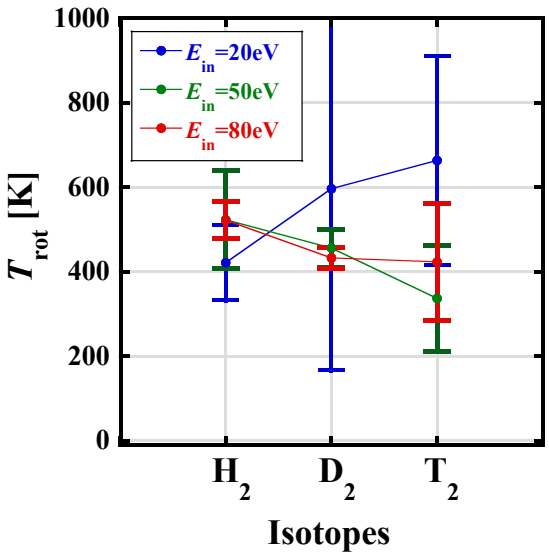

Fig. 9. Isotope effect of the rotational temperature. Evaluated rotational temperature T_{rot} of each kind of isotopic molecules is plotted. The error bars are given by fitting Eq. (3) with the least square method in Fig. 8. The T_{rot} for both E_{in} = 50 and 80 eV decreases as the mass of the molecule increases. However, for E_{in} = 20 eV, since the fitting error is too large, it is difficult to evaluate the mass dependence. The initial temperature of the target is set to 300K.

the behavior of the hydrogen atoms/molecules emitted from the wall as they propagate through the plasma while undergoing chemical reactions.

In this study, we prepared one initial structure for each isotope and investigated the atoms/molecules generated from it. It is difficult to investigate the distribution of atoms in a real material by experiment. Therefore, in order to compensate for the lack of initial structure information, it is necessary to prepare a large number of plausible initial structures on a computer to increase the statistics. In reality, handling a large number of initial structures is limited by computational resources. To overcome this problem, we are currently developing a method that uses machine learning and other techniques.

Acknowledgment

The research was supported by Grants-in-Aid for Scientific Research (C), Nos.18K11416, 19K03802 and 19K03800 from the Japan Society for the Promotion of Science, and by the NIFS Collaborative Research Programs NIFS20KKGS028 and NIFS20KNSS150.

References

1) K. Sawada, H. Nakamura, S. Saito, G. Kawamura, M. Kobayashi, K. Haga, T. Sawada, M. Hasuo, Contrib. Plasma Phys. **60**(2020) e201900153, doi:10.1002/ctpp.201900153.
2) S. Saito, H. Nakamura, K. Sawada, G. Kawamura, M. Kobayashi and H. Hasuo, Contrib. Plasma Phys. **60**(2020) e201900152, doi:10.1002/ctpp.201900152.
3) S. Saito, H. Nakamura, K. Sawada, M. Kobayashi, G. Kawamura and H. Hasuo, Plasma Fus. Res. **15**(2020) 240307, doi:10.1585/pfr.15.2403073.
4) G.F. Matthews, J. Nucl. Mater. **220-222** (1995)104.
5) W.L. Hsu, M. Yamada and P. J. Barret, Phys. Rev. Lett. **49**(1982) 1001.
6) N. Ohno, D. Nishijima, S. Takamura, Y. Uesugi, M. Motoyama, N. Hattori, H. Arakawa, N. Ezumi, S. Krasheninnikov, A. Pigarov and U. Wenzel, Nucl. Fusion **41**(2001)1055.
7) N. Ohno, Plasma Phys. Control. Fusion **59** (2017)034007.
8) N. Ohno and M. Seki and H. Ohshima and H. Tanaka and S. Kajita and Y. Hayashi and H. Natsume and H. Takano and I. Saeki and M. Yoshikawa and H. van der Meiden, Nucl. Mater. Energy **19**(2019)458.
9) B. Lipschultz, J. Goetz, B. LaBombard, G.M. McCracken, J.L. Terry, M. Graf, R.S. Granetz, D. Jablonski, C. Kurz, A. Niemczewski, and J.Snipes, J. Nucl. Mater. **220-222**(1995) 73.
10) B.L. Stansfield and F. Meo and G. Abel and C. Boucher and J.-L. Gauvreau and J.P. Gunn and E. Haddad and J.-L. Lachambre and J. Mailloux and R. Marchand and G. Ratel and N. Richard and M.M. Shoucri and B. Terreault and S. Beaudry and R. Dècoste and G.W. Pacher and W. Zuzak and J.D. Elder and P.C. Stangeby, J. Nucl. Mater. **241-243**(1997)739.
11) G. Federici, C. H. Skinner, J. N. Brooks, J. P. Coad, C. Grisolia, A. A. Haasz, A. Hassanein, V. Philipps, C. S. Pitcher, J. Roth, W. R. Wampler and D. G. Whyte, Nucl. Fusion **41** (2001)1967.
12) S. Potzel and M. Wischmeier and M. Bernert and R. Dux and H.W. ´uller and A. Scarabosio, J. Nucl. Mater. **438**(2013)S285.
13) H. Tanaka, N. Ohno, Y. Tsuji, S. Kajita, S. Masuzaki, M. Kobayashi, T. Morisaki, H. Tsuchiya, A. Komori, and the LHD Experimental Group, Phys. Plasmas **17**(2010)102509.
14) A. Loarte, B. Lipschultz, A. S. Kukushkin, G. F. Matthews, P. C. Stangeby, N. Asakura, G. F. Counsell, G. Federici, A. Kallenbach, K. Krieger, A. Mahdavi, V. Philipps, D.

Reiter, J. Roth, J. Strachan, D. Whyte, R. Doerner, T. Eich, W. Fundamenski, A. Herrmann, M. Fenstermacher, P. Ghendrih, M. Groth, A. Kirschner, S. Konoshima, B. LaBombard, P. Lang, A. W. Leonard, P. Monier-Garbet, R. Neu, H. Pacher, B. Pegourie, R. A. Pitts, S. Takamura, J. Terry, E. Tsitrone, ITPA Scrape-off Layer and Divertor Physics Topical Group, Nucl. Fusion 2007, 47, S203.

15) S.I. Krasheninnikov, A. Yu. Pigarov, D. A. Knoll, B. LaBombard, B. Lipschultz, D. J. Sigmar, T. K. Soboleva, J. L. Terry and F. Wishing, Phys. Plasmas **4**(1997)1638.
16) S.I. Krasheninnikov, A. Yu. Pigarov, D. J. Sigmar, Phys. Lett. A **214**(1996) 285.
17) N. Ohno, N. Ezumi, S. Takamura, S.I. Krasheninnikov and A. Yu. Pigarov, Phys. Rev. Lett. **81**(1998) 818.
18) J.L.Terry, B. Lipschultz, A. Yu. Pigarov, S. I. Krasheninnikov, B. LaBombard, D. Lumma, H. Ohkawa, D. Pappas, and M. Umansky, Phys. Plasma **5** (1998) 1759.
19) K. Sawada and M. Goto, Atoms **4** (2016) 29.
20) J. Robertoson, Surf. Coat. Technol. **50** (1992) 185.
21) A. Zeng, V. F. Neto, J. J. Gracio and Q. H. Fan, Diam. Relat. Mat. **43** (2014) 12.
22) H. Yamada , K. Tanaka, R. Seki, C. Suzuki, K. Ida, K. Fujii, M. Goto, S. Murakami, M. Osakabe, T. Tokuzawa, M. Yokoyama, M. Yoshinuma and LHD Experiment Group, Phys. Rev. Lett. **123**(2019)185001.
23) K. Tanaka, Y. Ohtani, M. Nakata, F. Warmer, T. Tsujimura, Y. Takemura, T. Kinoshita, H. Takahashi, M. Yokoyama, R. Seki, H. Igami, Y. Yoshimura, S. Kubo, T. Shimozuma, T. Tokuzawa, T. Akiyama, I. Yamada, R. Yasuhara, H. Funaba, M. Yoshinuma, K. Ida, M. Goto, G. Motojima, M. Shoji, S. Masuzaki, C.A. Michael, L.N. Vacheslavov, M. Osakabe and T. Morisaki, Nucl. Fusion **59**(2019) 126040.
24) S. Saito, A. M. Ito, A. Takayama, H. Nakamura, Jpn. J. Appl. Phys. **51** (2012) 01AC05.
25) J. Roth, E. Tsitrone, T. Loarer, V. Philipps, S. Brezinsek, A. Loarte, G. F. Counsell, R. P. Doerner, K. Schmid, O. V. Ogorodnikova, Plasm. Phys. Control. Fusion **50**(2008)103001.
26) T. Schwarz-Selinger, A. von Keudell, and W. Jacob, J. Appl. Phys. **86**(1999) 3988.
27) W. Jacob, Thin Solid Films **326**(1998)1.
28) M. Tokitani, N. Yoshida, S. Masuzaki, N. Noda, A. Sagara, H. Yamada, A. Komori and LHD experiment group, S. Nagata, B. Tsuchiya, J. Nucl. Mater. **415**(2011) S87.
29) M. Tokitani, S. Masuzaki, T. Murase and the LHD Experiment Group, Nuclear Materials and Energy **18** (2019) 23.
30) J. Jacquinot on behalf of the EURATOM-CEA Association, Nucl. Fusion **43** (2003)

1583.
31) M. Suzuki, J. Math. Phys. **26**(1985) 601, doi:10.1063/1.526596.
32) D. W. Brenner, O. A. Shenderova, J. A. Harrison , S. J. Stuart, B. Ni and S. B. Sinnott, J. Phys.: Condens. Matter **14**(2002) 783, doi:10.1088/0953-8984/14/4/312.
33) S. Saito, H. Nakamura and M. Tokitani, Jpn. J. Appl. Phys. **56**(2017) 01AF04, doi:10.7567/JJAP.56.01AF04.
34) B. R. Johnson, J. Chem. Phys. **67** (1977) 4086.